Title: Perovskite-perovskite tandem photovoltaics with ideal bandgaps

Authors: Giles E. Eperon[1,3],* Tomas Leijtens[2],* Kevin A. Bush[2], Thomas Green[1], Jacob Tse-Wei Wang[1], David P. McMeekin[1], George Volonakis[4], Rebecca L. Milot[1], Daniel J. Slotcavage[2], Rebecca Beslile[2], Jay B. Patel[1], Elizabeth S. Parrott[1], Rebecca J. Sutton[1], Wen Ma,[5] Farhad Moghadam,[5] Bert Conings[1,6], Aslihan Babayigit[1,6], Hans-Gerd Boyen[6], Feliciano Giustino[4], Laura M. Herz[1], Michael B. Johnston[1], Michael D. McGehee[2] and Henry J. Snaith[1]

*GEE and TL contributed equally to this work.

Correspondence to: MDM (mmcgehee@stanford.edu), HJS (henry.snaith@physics.ox.ac.uk)

Affiliations:

[1]Department of Physics, University of Oxford, Clarendon Laboratory, Parks Road, Oxford OX1 3PU, UK

[2]Department of Materials Science, Stanford University, Lomita Mall, Stanford, CA, USA

[3]Department of Chemistry, University of Washington, Seattle, WA, USA

[4]Department of Materials, University of Oxford, Parks Road, Oxford OX1 3PH, UK

[5]SunPreme, Palomar Avenue, Sunnyvale, CA, USA

[6]Institute for Materials Research, Hasselt University, Diepenbeek, Belgium

Abstract:

Multi-junction solar photovoltaics are proven to deliver the highest performance of any solar cell architecture, making them ideally suited for deployment in an increasingly efficiency driven solar industry. Conventional multi-junction cells reach up to 45% efficiency, but are so costly to manufacture that they are only currently useful for space and solar concentrator photovoltaics. Here, we demonstrate the first four and two-terminal perovskite-perovskite tandem solar cells with ideally matched bandgaps. We develop an infrared absorbing 1.2eV bandgap perovskite, $FA_{0.75}Cs_{0.25}Sn_{0.5}Pb_{0.5}I_3$, which is capable of delivering 13.6% efficiency. By combining this material with a wider bandgap $FA_{0.83}Cs_{0.17}Pb(I_{0.5}Br_{0.5})_3$ material, we reach initial monolithic two terminal tandem efficiencies of 14.0 % with over 1.75 V open circuit-voltage. We also make mechanically stacked four terminal tandem cells and obtain 18.1 %

efficiency for small cells, and 16.0 % efficiency for 1cm^2 cells. Crucially, we find that our infrared absorbing perovskite cells exhibit excellent thermal and atmospheric stability, unprecedented for Sn based perovskites. This device architecture and materials set will enable "all perovskite" thin film solar cells to reach the highest efficiencies in the long term at the lowest costs, delivering a viable photovoltaic technology to supplant fossil fuels.

One Sentence Summary: We have designed narrow-bandgap perovskite compositions allowing us to make efficient all-perovskite tandem solar cells with ideal bandgaps, for the next generation of low cost and high efficiency solar cells.

Main text:

Recently, metal halide perovskites have received considerable attention in the photovoltaic (PV) community due to their rapidly increasing power conversion efficiencies (PCEs) and low processing costs. These perovskites are solution-processable semiconductors with the formula ABX_3, where generally A = Cs, methylammonium (MA), or formamidinium (FA), B = Pb or Sn, and X = I, Br, or Cl; changing the components in the lattice tunes the bandgap. Single junction perovskite devices have reached a certified 22% PCE, reaching ever closer to the best reported efficiencies of silicon-based devices.(*1*) While this is promising, the total system costs for PV installations mean that the module efficiency of any technology has to be extremely high to be able to compete favorably with electricity produced from coal power plants. It now seems likely that the first commercial iteration of a perovskite device will be as an "add-on" to silicon photovoltaics, in a tandem configuration, where a ~1.75eV perovskite material can enhance the efficiency of the silicon cell to a possible 30%, allowing the new perovskite technology to benefit from the existing value chain and scale of the silicon PV industry.(*2*) However, this approach forsakes the ultimate attraction of perovskites, which is high volume thin film manufacture via inexpensive solution or vapor phase processing. Since glass, encapsulation and electrical wiring and connection out of a module remain the most expensive parts of the module,(*3*) and the module is only around 50% of the cost of the PV installation, increased cell efficiency (power output per unit area) is the key drive to cost reduction. Hence, a perovskite-only technology will have to match or surpass the efficiency of both silicon and at least match perovskite-on-silicon tandems before it is feasibly commercial. Ironically, the foreseen success of the perovskite-on-silicon tandem approach will raise the efficiency bar for perovskite-only PV deployment. Therefore, an apparent solution is to develop all perovskite multi-junction cells, which could eventually surpass 40% efficiency, as has already been achieved with triple and 5 junction III-V semiconductor cells.(*4*)

So far, efficient perovskite devices have only been reported with Pb-based materials, which have bandgaps that cannot be tuned to below 1.48 eV. For the highest efficiency tandem device, a combination of a 0.9-1.2 eV rear cell and a corresponding 1.7-1.9 eV front cell is desired.(*5*) Our recent work on $FA_{0.83}Cs_{0.17}Pb(I_xBr_{1-x})_3$ has shown that it is possible to make stable and efficient perovskite materials with appropriate bandgaps for the front cell.(*2*) Thus, making an efficient low bandgap material is of paramount importance to enabling high performance perovskite tandems. By completely replacing the Pb with Sn, the bandgap can be shifted to ~1.3eV (for $MASnI_3$).(*6*) However, the tin-based materials are notoriously air-sensitive and difficult to process, meaning that devices have been limited to ~6% PCE.(*6*, *7*) Notably, recent work reports an anomalous bandgap bowing in tin-lead mixed perovskite systems, resulting in a bandgap tunable down to ~1.2eV with $MAPb_{0.5}Sn_{0.5}I_3$. While this should make an ideal bandgap material for the rear cell of a tandem device, the performances so far have been mediocre (~7% PCE), likely due to processing difficulties and poor stability.(*8*) The best results reported so far in Sn-Pb mixed perovskites (10 % PCEs) were obtained with materials incorporating only 10 % Sn content, which exhibit bandgaps around 1.3 eV, non-ideal for use in all-perovskite tandems.(*9*) Moreover, due to the short charge carrier diffusion lengths reported thus far in the Sn based perovskites, most device work has been done in the mesoporous titania architecture, where carriers are rapidly extracted from the perovskite over several nm length scales into mesoporous titania. This is not ideal for either low temperature processing (typically requires sintering at 500 °C) or for long-term stability under solar illumination.(*6*, *10*) Specifically concerning Sn perovskites, it is thought that self-doping due to tin vacancies or Sn^{4+} generation causes very rapid recombination in the perovskite.(*6*, *11*) It is possible that further material defects can be induced by heating, where SnI_4 gas will be driven off leaving a non-stoichiometric material, or exposure to oxygen/water, causing Sn^{2+} to oxidize to Sn^{4+}.(*12*)

In addition to the previous lack of efficient low gap perovskites, monolithic perovskite tandems are notoriously difficult to fabricate simply because the multiple layers are typically solution processed from highly coordinating solvents, and their subsequent coating dissolves the underlying layers. While interesting results have been obtained by "gluing" a $CH_3NH_3PbBr_3$ and a $CH_3NH_3PbI_3$ cell together, a reproducible, scalable, and high performance perovskite tandem has not been reported.(*13*)

Here, we firstly demonstrate a stable and efficient perovskite material with a 1.2eV bandgap, realized with a formamidinium-based mixed tin-lead iodide perovskite. We use the formamidinium cation rather than methylammonium due to its superior stability.(*14*) With a novel processing technique we are able to fabricate smooth and uniform planar layers of $FAPb_x,Sn_{1-x}I_3$ perovskites, and observe an anomalous bandgap trend, similar to that previously observed with $MAPb_x,Sn_{1-x}I_3$, resulting in bandgaps tunable between 1.2 and 1.48eV. We take the 1.2eV material, and improve it further by incorporating some cesium, fabricating $FA_{0.75}Cs_{0.25}Pb_{0.5}Sn_{0.5}I_3$, which also has a 1.2 eV bandgap. Unprecedented for these Sn based materials, we show long diffusion lengths due to high charge carrier mobilities. This allows us to prepare working simplified and low temperature planar heterojunction PV devices with high efficiencies (10 and 13.6 % for the $FAPb_{0.5}Sn_{0.5}I_3$ and $FA_{0.75}Cs_{0.25}Pb_{0.5}Sn_{0.5}I_3$, respectively) and impressive V_{OC}s of up to 0.79 V. We demonstrate surprisingly good thermal and air- stability despite the inclusion of tin in the perovskite, promising for long-term operation.

Secondly, we fabricate efficient 1.8 eV perovskite cells employing $FA_{0.83}Cs_{0.17}Pb(I_{0.5}Br_{0.5})_3$, tuned to current match the low bandgap perovskite in a tandem architecture. We use a sputtered ITO interlayer as both the recombination layer and as a protective barrier to allow us to solution process the second perovskite cell on top of the first. Using these two new materials and the new architecture, we demonstrate the feasibility of making current matched and efficient (14 %) monolithic all-perovskite tandem solar cells on small areas and 12.6 % on large areas, with open-circuit voltages exceeding 1.75 V. We also fabricate 18.1 % efficient small area cells and 16.0 % efficient 1cm^2 all-perovskite four terminal tandems using a semitransparent 1.6eV $FA_{0.79}MA_{0.16}Cs_{0.05}Pb(I_{0.83}Br_{0.17})_3$ front cell. As the subcells continue to improve in performance in the same way that other FA and MA based perovskite cells have, we expect the perovskite tandems made as we describe here to approach 30 % power conversion efficiencies and provide a thin-film PV technology with an unprecedented combination of high performance and low cost.

Results and discussion

We and others have observed that is it difficult to fabricate a smooth, pinhole-free layer of tin-based perovskites on planar substrates.(*6*, *7*) We found that this difficulty is maintained for the Sn-Pb mixed materials. However, obtaining such a layer is a key step in fabricating a high quality photovoltaic device.(*15*, *16*) We therefore initially develop a new deposition technique to allow formation of high quality Sn-Pb mixed perovskites. The poor film quality appears to stem from the fact that the tin-based perovskites crystallize much more rapidly, forming upon spin-coating when a 1:1 MAI:SnI_2 or FAI:SnI_2 solution in DMF is utilized, resulting in very rough films. This problem also affected our attempts to use a two-step deposition technique in a similar manner to that used with the Pb perovskites, as we show in Fig S1. Moreover, recent work suggests that heating tin-based perovskites above 100 °C will result in material degradation due to oxidation and release of the tin as SnI_4 gas - ideally the deposition would not involve heating the film.(*12*) We thus developed a new technique to deposit tin-containing perovskites, $FASn_xPb_{1-x}I_3$, incorporating elements of two previous techniques: the use of low vapor pressure solvents to retard crystallization by forming precursor complexes, and the use of an “anti-solvent” bath to crystallize the film with only gentle heating.(*7*, *17*) Rather than using pure DMSO as a solvent,(*7*) we find that in order to form a uniform film on a planar substrate a mixture of DMSO and DMF is ideal. Spin-coating a precursor dissolved in a DMSO-DMF mixture results in a uniform film that is not yet fully crystallized - it has a transparent appearance, presumably due to the presence of coordinated DMSO-SnI_2 complexes. To crystallize the films, we rapidly immerse them in an anti-solvent bath; we find anisole to be the most effective anti-solvent here (as we show in Fig. S2), which is conveniently relatively non-toxic and acceptable for use in manufacturing.(*18*) We observe that the films rapidly change color to deep reddish upon immersion in the anti-solvent. Via FTIR analysis (see Fig. S5) we observe some residual DMSO still present in the as formed films, suggesting the presence of a DMSO complex precursor phase.(*19*) Subsequent annealing at 70 °C removes this DMSO, and we can form smooth, dark, highly crystalline and uniform $FASn_xPb_{1-x}I_3$ films over the entire range of values of x = 0 to 1, as we show for a selection of materials in Fig. 1a. We note that only the pure Pb material required heating at a higher temperature (170 °C) to convert the film from the yellow room-temperature phase to the black phase.(*12*) We term this deposition technique “Precursor-phase Anti-solvent Immersion” or PAI.

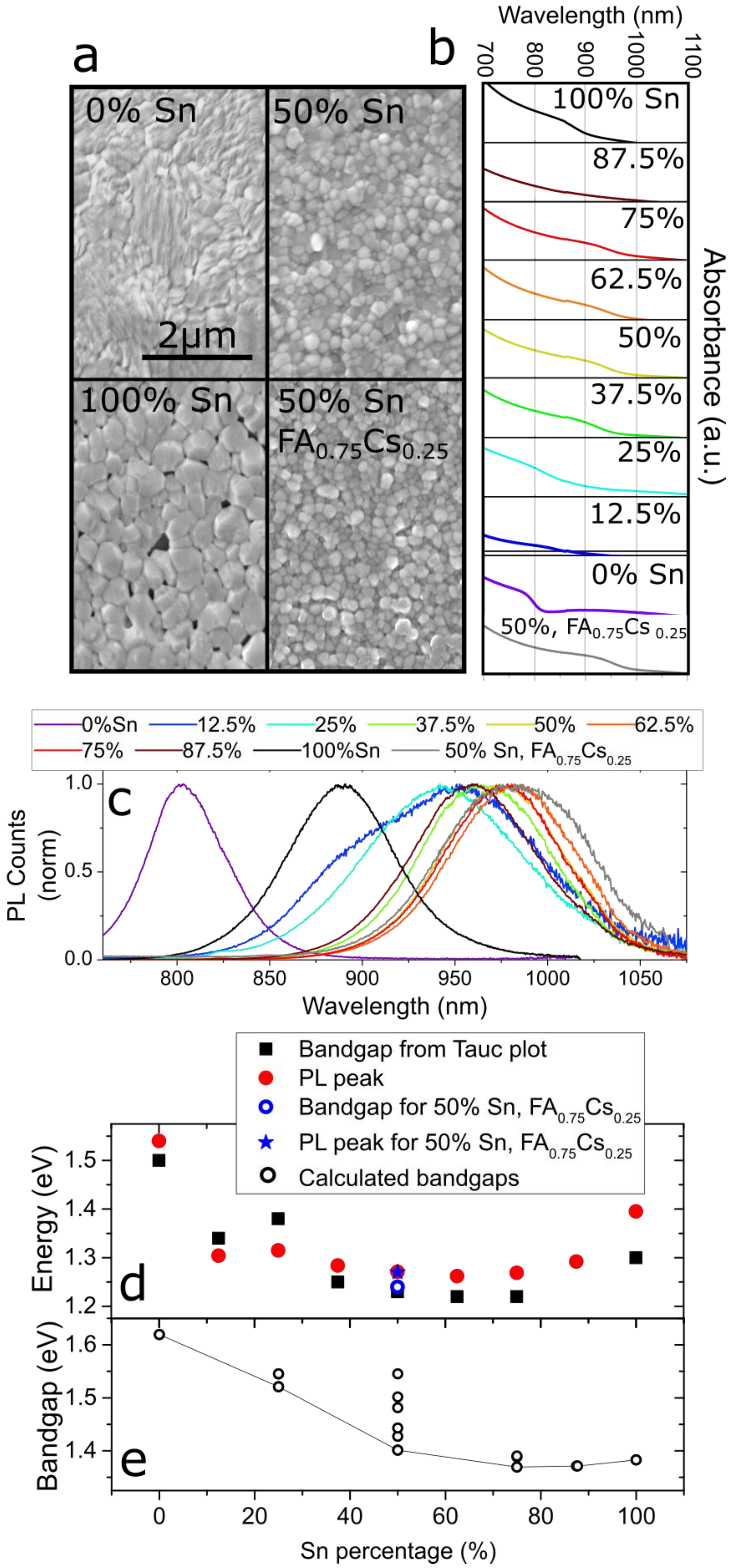
a
0% Sn
50% Sn
2μm
100% Sn
50% Sn $FA_{0.75}Cs_{0.25}$
b
Wavelength (nm)
700
800
900
1000
1100
100% Sn
87.5%
75%
62.5%
50%
37.5%
25%
12.5%
0% Sn
50%, $FA_{0.75}Cs_{0.25}$
Absorbance (a.u.)
0%Sn
12.5%
25%
37.5%
50%
62.5%
75%
87.5%
100%Sn
50% Sn, $FA_{0.75}Cs_{0.25}$
c
PL Counts (norm)
1.0
0.5
0.0
800
850
900
950
1000
1050
Wavelength (nm)
Bandgap from Tauc plot
PL peak
Bandgap for 50% Sn, $FA_{0.75}Cs_{0.25}$
PL peak for 50% Sn, $FA_{0.75}Cs_{0.25}$
Calculated bandgaps
Energy (eV)
1.5
1.4
1.3
1.2
d
Bandgap (eV)
1.6
1.5
1.4
e
0
20
40
60
80
100
Sn percentage (%)

Figure 1: Tin-lead alloying *a) Scanning electron microscope (SEM) images showing the top surface of* $FASn_xPb_{1-x}I_3$ *films with different Sn percentages and* $FA_{0.75}Cs_{0.25}Pb_{0.5}Sn_{0.5}I_3$ *(discussed later, and labelled here as "50%,* $FA_{0.75}Cs_{0.25}$*"), fabricated with the PAI deposition technique. The 0% Sn films was subsequently annealed at 170 ºC, the others at 70 ºC. b) Absorption spectra of* $FASn_xPb_{1-x}I_3$ *films with varying Sn % and* $FA_{0.75}Cs_{0.25}Pb_{0.5}Sn_{0.5}I_3$*. C) Photoluminescence spectra of* $FASn_xPb_{1-x}I_3$ *films with varying Sn% and* $FA_{0.75}Cs_{0.25}Pb_{0.5}Sn_{0.5}I_3$*. D) Plot of experimentally estimated bandgap as a function of Sn %, determined from absorption onset in a Tauc plot (assuming direct bandgap) of the absorption (black); PL peak positions are given in red. e) Bandgaps for a Sn-Pb perovskite alloys calculated from first principles using a supercell containing eight* BX_6 *octahedra, where the Sn and Pb atoms are ordered relative to each other (See SM for full details). Points plotted represent all possible bandgaps for a particular composition, based on all possible Sn-Pb configurations; a solid line is drawn through the lowest bandgap options as a comparison to experiment.*

Having developed a route to produce continuous and smooth planar films of $FASn_xPb_{1-x}I_3$, we now compare the material properties across the whole series, to determine if the anomalous bandgap behavior observed in the MA analogue is also present in the FA system. In Fig. 1 b and c we show photoluminescence spectra and absorption spectra of a range of compositions. From this data, the optical bandgap can be estimated from Tauc plots (from absorption), and the PL peak positions; we show the combined extracted values of bandgap in Fig. 1d. It is immediately apparent that although the neat $FAPbI_3$ and $FASnI_3$ materials show bandgaps consistent with previously reported values, ~1.5eV and ~1.3eV respectively, the mixed materials do not follow the linear intermediate behavior expected from Vegard's law. Instead, we observe that the bandgap narrows in between the two endpoints, similar to the observations of Kanatzidis et al. with the MA system.(*8*) Importantly, at compositions of 50-75% Sn, the bandgap narrows to almost 1.2eV. X-ray diffraction spectra, which we show in Fig S4, for the whole series, show that there is only a single dominant perovskite phase present, demonstrating that a solid solution or alloy is formed rather than a mixture of two materials. We fitted the X-ray data to determine the unit cell parameters, as we detail in Table S1. In accordance with literature, the neat Pb material fits a trigonal structure well, and the neat Sn a cubic phase.(*12*) We note that here the PL peaks appear to be higher in energy than the absorption onset. This is commonly observed for the other Pb based perovskite semiconductors and is beneficial for the photovoltaics, since the PL peak position is indicative of the average energy of the recombining electrons and holes. Therefore the PL peak siting close to, or even slightly higher energy than the optical bandgap determined by the absorption onset indicates no systematic energy loss in the material, and highlights that in the thermodynamic "radiative limit", where all electron and hole recombination is via radiative decay, the material should operate extremely efficiently in a solar cell.(*20*, *21*) We note that we also present data for a mixed FA-Cs cation perovskite in Fig 1. We find that the measured material properties appear similar to the pure FA perovskite, and we discuss implications to device performance in a later section.

In order to elucidate the mechanisms underpinning this anomalous bandgap trend, we perform first-principles calculations of bandgaps as a function of the tin-lead ratio. We provide complete details on the computational methods in the SM. We take two approaches, approximating firstly a random solid solution with Pb and Sn in effectively random locations, and secondly an ordered structure, where the Sn and Pb atoms occupy a specific position relative to each other within a repeating lattice unit of eight octahedra. This 'supercell' approach allows us to investigate the role of local ordering in the Pb and Sn cation positions. Using the random solid solution approach, we find that bandgap decreases monotonically, as we show in Fig. S6, inconsistent with our experiments. On the other hand, when taking the supercell approach and placing Pb and Sn atoms in certain configurations within the lattice, and taking the lowest bandgaps for each ratio, an anomalous bandgap trend emerges, as we show in Fig. 1e. For compositions with more than 50% Sn, a specific type of short-range order in the Pb-Sn positions allows the bandgap to dip below the end points, as we observe experimentally. We thus postulate that a local ordering in this manner is likely to be responsible for the anomalous bandgap trend. This ordering is on the length-scale of two to three lattice octahedra. Recently, Im et al. attributed a similar anomalous bandgap trend observed for $MAPb_xSn_{1-x}I_3$ to the competition between spin-orbit coupling and distortions of the lattice.(*22*) However, if this was the case here, we would have observed it in the random solid solution approach. Therefore our results lead us to believe that "spin-orbit antagonism" is not the root cause of the anomalous bandgap trend. We also highlight that the energetic difference between the various Pb-Sn configurations which we calculate is on the order of 2meV, so at room temperature the materials are likely to contain various combinations of the configurations which we show in Fig. S6, but the absorption and emission onsets probed by UV-VIS and PL reflect the ones with the smallest gap. This could explain the shallow absorption edge and broad PL peaks we observe for many of the materials. We also note that the short-range order we propose is on the sub-nm regime, and thus fully compatible with sample homogeneity at the nano- and micro-scales.

In order to determine the diffusion length, mobility and recombination lifetimes of these materials we perform optical pump-probe THz spectroscopy, a noncontact method for measuring photoinduced conductivity and charge-carrier mobility, on $FASnI_3$ and $FASn_{0.5}Pb_{0.5}I_3$. We show the fluence dependence of the THz transients for $FASn_{0.5}Pb_{0.5}I_3$ in Fig. S7, which exhibit faster decays at higher intensities as the result of increased bimolecular and auger recombination.(*23*) From this data, we calculate the rate constants of the different recombination mechanisms (1st, 2nd and 3rd order) along with the charge-carrier mobility. Encouragingly, we determine the charge-carrier mobility of $FASnI_3$ and $FASn_{0.5}Pb_{0.5}I_3$ to be 22 $cm^2V^{-1}s^{-1}$ and 17 $cm^2V^{-1}s^{-1}$ respectively. This is significantly higher than the value we previously determined for $MASnI_3$, which was only 2 $cm^2V^{-1}s^{-1}$, and within the range of ~15-30 $cm^2V^{-1}s^{-1}$, which is typical for the Pb based perovskite films including $FAPbI_3$.(*24*, *25*) This demonstrates that, firstly this deposition method for the Sn based perovskites results in high charge carrier mobility materials, and secondly, the mixed-metal compositions do not suffer from electronic disorder (which would limit the mobility), rather, it has a similar high mobility as the neat materials. We now estimate the charge-carrier diffusion as we detail in the SM; we find that for charge-carrier densities typical under solar illumination, a value of ~ 300nm is reached for the composition $FASn_{0.5}Pb_{0.5}I_3$. This is lower than for the best reported perovskite materials, but importantly it is equivalent to the typical thickness required to absorb most incident light (~300-400nm), meaning that a simple planar perovskite cell should be able to extract most photo-generated charge effectively.(*26*) The diffusion length is still limited by very short carrier lifetimes on the order of 1-2 ns, suggesting that there is ample room for improvement by further minimizing defect densities and self-doping.

To assess solar cell performance over the $FASn_xPb_{1-x}I_3$ range of materials, we fabricated a series of planar heterojunction devices in the 'inverted' p-i-n architecture.(*27*) The architecture comprises ITO/PEDOT:PSS/$FASn_xPb_{1-x}I_3$/C_{60}/BCP capped with an Ag or Au electrode, as illustrated in Fig. 2a. We show the current-density voltage (J-V) curves and external quantum efficiency (EQE) measurements for the whole compositional series in Fig. S8. The onset of the EQEs closely matches that of the absorption of the materials, with light harvested out to ~1020nm in the 50%-75% Sn compositions. Remarkably, with this deposition process we are also able to generate a significant short-circuit current from the pure Sn planar devices, which has never been reported before; they have only previously worked when combined with mesoporous TiO_2 in a mesostructured device, to compensate for short charge carrier diffusion lengths. The highest efficiencies are generated from the devices with 50% Sn, which lies within the lowest bandgap region, so we then take this as the best material to optimize for low-gap solar cells.

As a means of further enhancing the performance of the low-bandgap cells, we investigate the impact of a small addition of Cs, which has recently been found to boost the performance of Pb based perovskites.(*28*–*30*) Substituting 25% of the FA with Cs results in films with very similar properties- bandgap, morphology, photoluminescence, crystal structure, and charge carrier diffusion lengths remain almost unchanged, as we show in Fig. 1, Fig. S4, and Fig. S7. We show current-voltage characteristics and stabilized power output for the best devices in Fig. 2b and 2c respectively. For the champion $FAPb_{0.5}Sn_{0.5}I_3$ device, a current-voltage scanned short-circuit current of 22 $mAcm^{-2}$, V_{oc} of 0.70 V and FF of 0.66 combine to give an efficiency of 10.2 %. We observe little hysteresis between forward and reverse JV fast scans, and the stabilized power output is close to (in fact greater than) the JV scan efficiency, at 10.9%. Upon substituting 25% of the FA for Cs, we observe substantial improvements in solar cell performance, illustrated by the batch statistics which we show in Figure S10. For the champion device, we observe a short-circuit current of 25 $mAcm^{-2}$, V_{oc} of 0.75 V, and a fill factor of 0.72 to yield 13.6 % PCE. We plot the EQEs of the two materials in Figure 2d, and find that the scanned current densities correspond well to those obtained by integrating the EQEs over the solar spectrum. Both devices produce photocurrent out to 1020 nm, but the Cs containing material displays a significantly higher EQE throughout the entire spectral range. It also appears that these cells suffer from an interference fringe at around 700 nm, which implies that further improvements in light harvesting should be possible through careful modeling and design of the optical stack. We performed UPS and XPS measurements to determine the energetic positions of the conduction and valence bands for a selection of compositions, shown in Fig S10, and we find that the band levels for $FASn_{0.5}Pb_{0.5}I_3$ are extremely well placed for the choice of C_{60} and PEDOT:PSS as electron and hole acceptors, consistent with the impressively high voltages and low loss-in-potential we have attained. The Cs-containing material shows an energetically shallower valance band and mild p-type doping, which could account for the enhanced device performance via better energetic alignment with PEDOT:PSS.(*31*, *32*)

A fundamental measure of the electronic losses in a solar cell is the difference in energy between the bandgap of the absorber, and the open-circuit voltage a solar cell generates, often termed the loss-in-potential.(*33*) For crystalline silicon PV cells, which generate a record V_{oc} of 0.74 V and have a bandgap of 1.14eV, this loss is 0.4V.(*4*) Some of our $FA_{0.75}Cs_{0.25}Sn_{0.5}Pb_{0.5}I_3$ devices here displayed V_{oc}s up to 0.79 V (as shown in Fig. S9), with a 1.2 eV bandgap, closely matching the loss of ~0.4V of crystalline silicon. The maximum possible values for J_{sc} and V_{oc}, according to a Shockley-Quiessier calculation for a 1.2 eV material are 38.7 $mAcm^{-2}$ and 0.97 V. Therefore, there remains room for improvement, but these relatively high V_{oc} and substantial performance already imply that when properly optimized this low bandgap perovskite should at least match the efficiency of the best silicon PV cells.

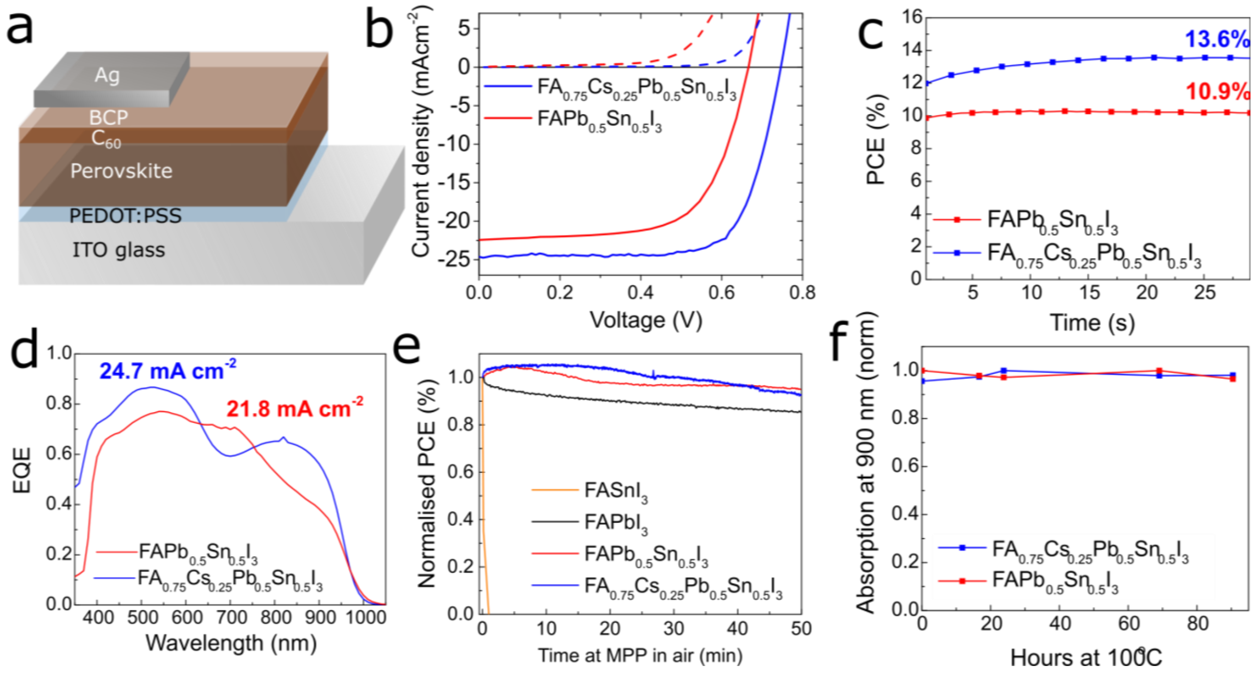

Fig. 2. Performance and stability of $FASn_{0.5}Pb_{0.5}I_3$ and $FA_{0.75}Cs_{0.25}Sn_{0.5}Pb_{0.5}I_3$ perovskite solar cells. *a) Schematic of the device architecture for narrow-gap single junction perovskite solar cells. b) Current-voltage characteristics under AM1.5G illumination for the champion $FASn_{0.5}Pb_{0.5}I_3$ and $FA_{0.75}Cs_{0.25}Sn_{0.5}Pb_{0.5}I_3$devices under illumination (solid lines) and in the dark (dotted lines), measured at 0.38V/s with no pre-biasing or light soaking. c) Champion solar cell stabilized power outputs, measured via a maximum power point tracking algorithm. d) External quantum efficiency for representative devices with the integrated current shown as an inset, providing a good match to the J-V scan J_{sc}. e) PCE as a function of time for three compositions of $FASn_xPb_{1-x}I_3$ (x=0, 0.5, 1) as well as $FA_{0.75}Cs_{0.25}Sn_{0.5}Pb_{0.5}I_3$ measured by holding the cell at maximum power point in air under AM1.5 illumination. f) Thermal stability of $FASn_{0.5}Pb_{0.5}I_3$ and $FA_{0.75}Cs_{0.25}Sn_{0.5}Pb_{0.5}I_3$ films, quantified by heating the samples at 100 °C and monitoring their absorption at 900 nm as a function of time.*

	J_{SC} (mA cm^{-2})	V_{OC} (V)	FF	PCE (%)	SPO (%)
$FASn_{0.5}Pb_{0.5}I_3$	21.9	0.70	0.66	10.2	10.9
$FA_{0.75}Cs_{0.25}Sn_{0.5}Pb_{0.5}I_3$	25.1	0.75	0.72	13.6	13.6

Table 1. *Device parameters corresponding to the J-V curves in Figure 1a.*

Tin based perovskites have previously been observed to be extremely unstable in air; the Sn^{2+} can be oxidized to Sn^{4+}, resulting in the formation of SnI_4 gas, Sn-vacancy generation and ultimately complete deterioration of the films.(*34*) Water in the air may also hydrate the perovskite crystal structure, which weakens hydrogen bonding between the organic cation and the inorganic octahedral and is likely to facilitate Sn^{2+} oxidation.(*35*) As a result, the stability of such devices is a key concern, especially if they are to be incorporated into commercial perovskite tandem modules. In order to assess the stability of the $FASn_{0.5}Pb_{0.5}I_3$ and $FA_{0.75}Cs_{0.25}Pb_{0.5}Sn_{0.5}I_3$ devices compared to $FASnI_3$ and $FAPbI_3$, we carried out a simple aging test; holding the devices at maximum power point under $100mWcm^{-2}$ illumination and measuring power output over time in ambient air with a relative humidity of 50±5%. We show the results in Fig. 2e. As anticipated, the $FASnI_3$ device degrades in a matter of seconds after exposure to air. The $FAPbI_3$ device maintains its performance relatively well with a small drop observed over the time, possibly associated with photo-oxidation and hydration of the un-encapsulated perovskite layer, or a partial reversion to the yellow room-temperature phase.(*36*, *37*) Importantly, both the $FASn_{0.5}Pb_{0.5}I_3$ and $FA_{0.75}Cs_{0.25}Sn_{0.5}Pb_{0.5}I_3$ devices maintain their performance very well over this time, showing similar or even better stability than the neat Pb material. This is quite unprecedented; the inclusion of tin is expected to reduce the material stability dramatically. However, it appears that here, as well as in the case of the diffusion length, the mixed Sn:Pb composition retains the beneficial attributes of the neat Pb material.(*8*) As an additional stress test, we subject bare perovskite films to thermal stressing under nitrogen, heating for a long time at 100 °C. We monitor their absorption spectra in situ to determine whether the optical quality of the materials is degrading.(*38*) As we show in Figure 2f, the $FAPb_{0.5}Sn_{0.5}I_3$ and $FA_{75}Cs_{25}$ $Pb_{0.5}Sn_{0.5}I_3$ materials show no signs of decomposition over the course of four days at 100 °C, demonstrating that the material does not undergo a thermally induced degradation to PbI_2 and suggesting that there is not large scale evolution of SnI_4 gas. Because significant defect formation may not initially be visible in absorption spectra, we have also monitored the performance of full devices at 85 °C over several months (Figure S11). We find that here, too, the Sn:Pb material displays similar device stability as the pure Pb material. The outstanding performances in our preliminary atmospheric and thermal stability tests are an indication that these Sn:Pb materials do not suffer from some of the common atmospheric and thermal stability problems of other perovskite materials, and are likely to be viable for real world applications.

The motivation for developing a 1.2eV perovskite is for application in tandem devices. A 1.2eV perovskite is ideally suited as the rear cell in either monolithic two terminal (2T) tandem solar cells or mechanically stacked four terminal (4T) tandem solar cells. The architectures of the two types of tandems are depicted schematically in Figure 3a. A 2T tandem benefits from being monolithically integrated and has few parasitically absorbing layers, giving it the potential for the highest performance. However, because the two cells are connected in series, using a recombination layer in the middle, they must be perfectly current matched to deliver the optimum performance. A 4T tandem, on the other hand, is not limited by the current matching requirement as the two cells can be operated independently, or the areas of each subcell in the modules can even be tuned to ensure current matching in the actual module.(*39*) This system will also be advantageous when the sun's irradiation does not perfectly match AM1.5, when a 2T tandem will be limited by one of the subcells. The disadvantage of the 4T system is the use of an extra transparent electrode which can result in more absorption losses. We plot the theoretical efficiencies of both 2T and 4T tandems using a 1.2eV rear cell in Figure S12, and show that the 2T architecture requires the use of a top cell with a ~1.75-1.85eV bandgap to benefit from the tandem architecture and deliver a theoretical > 38 % efficient tandem with a very steep drop in performance as the front cell deviates from those bandgaps. The 4T architecture has a much more relaxed requirement on the front cell bandgap; front cells with 1.6-1.9eV are all capable of delivering >38 % efficient 4T tandems with the 1.2eV rear cell.

We have recently demonstrated a route to obtaining efficient and stable perovskites with appropriate wide bandgaps for front cells in tandem architectures by using a mixture of formamidinium and cesium cations.(*2*) The bandgap is controlled by tuning the Br:I ratio in $FA_{0.83}Cs_{0.17}Pb(I_xBr_{1-x})_3$ where x=0.5 yields a material with a 1.8 eV bandgap, ideally suited as the front cell in a 2T tandem with our 1.2eV perovskite. Here, we applied the PAI deposition route for the wide gap material to form smooth and thick (400-500 nm) perovskite layers. This yields efficient devices (~10-12 %) with appropriate photocurrents (up to 14-16 mA cm^{-2}) and voltages (1.0 - 1.1 V), making this material promising for use as the front cell in the perovskite tandem (see Fig. S13 for device performance data and stability). We note that the V_{OC}s we observe here for our wide bandgap cells are lower than we have previously reported for $FA_{0.83}Cs_{0.17}Pb(I_xBr_{1-x})_3$.(*2*) This is due to our use of the "inverted" p-i-n architecture here, which we have found to be more ideal for the Sn-based perovskite cells, and as we will show below is compatible with 2T tandem cell integration. At present this architecture delivers lower than ideal voltages with the Pb based perovskite cells.

For the recombination layer between the two sub-cells, we employ a double layer of aluminum doped zinc oxide nanoparticles (AZO NPs) coated with sputter coated indium tin oxide (ITO) between the 1.8 eV and 1.2 eV perovskites solar cells.(*40*) As we show in Fig S14, this thick ITO layer completely protects the underlying perovskite solar cell from any solvent damage, so we simply fabricate the 1.2 eV $FA_{0.75}Cs_{0.25}Sn_{0.5}Pb_{0.5}I_3$ solar cell directly on top. Its high conductivity for both electrons and holes facilitates effective recombination as desired. The AZO NPs protect the perovskite cell from damage during sputtering, as we have previously detailed.(*40*) We show a color enhanced SEM image of the full tandem device in Figure 3b.

We observe remarkably good performance of the tandem solar cells, which deliver power conversion efficiencies in excess of either of the individual subcells. We plot the JV curves of the best single junction Pb:Sn cells, the best single junction 1.8 eV cell (with transparent ITO top electrode), and that of the best 2T tandem device of the same batch in Figure 3c. We note that none of the devices exhibit significant hysteresis in the JV curves, as confirmed by the power output over time plotted in Figure 3g. The photocurrent of the tandem solar cell is at 12.5 mA cm^{-2}, half the photocurrent of the isolated low bandgap rear cell, indicating that we have indeed made two subcells that are well current matched. We confirm the photocurrent output of the devices via EQE measurements (Fig. 3d), which demonstrate that the 1.2 eV subcell is limiting the photocurrent, but only by a small margin. The voltage is an appropriate addition of the two subcells (1.76 V), but the fill factor is limited to 0.6, yielding an overall performance of 13.4 % via a scanned JV curve but of 13.9 % when stabilized at its maximum power point.

The monolithic tandem is mainly limited by the low photovoltage of the 1.8 eV cell; only at 1.09 V. This represents a 0.71V loss-in-potential, which is a much larger loss than that obtained for most well optimized perovskite cells (0.4-0.5 V). To mitigate such losses, we made semi-transparent solar cells using a 1.6 eV $FA_{0.79}MA_{0.16}Cs_{0.05}Pb(I_{0.83}Br_{0.17})_3$ perovskite, similar to that reported recently by Saliba et al,(*41*) but with a transparent ITO top contact, and we obtain a 14.1 % efficient solar cell with a V_{oc} over 1 V. A 1.6 eV material is of course not suitable for a 2T tandem with a 1.2 eV rear cell, but it is very well suited to be an efficient top cell in a mechanically stacked 4T tandem, as discussed above. Indeed, when we filter a 13.1 % $FA_{0.75}Cs_{0.25}Sn_{0.5}Pb_{0.5}I_3$ cell with the 14.1 % 1.6 eV cell, we can still extract substantial photocurrent (7.7 mA cm^{-2}) and power (4.0 mW cm^{-2}) from the low-bandgap device. We plot the JV curves and EQE spectra of the 1.6 and 1.2 eV cells in the 4T tandem in Fig 3e-f and show that it is possible to obtain an additional 4.0 % PCE from the 1.2 eV rear cell, yielding an overall tandem efficiency of 18.1 %, as shown in Fig. 3g.

While very high efficiencies have been reported for perovskite solar cells, these are mainly on very small (often <0.1cm^2) devices. Our results so far have been on 0.2cm^2 devices. To prove that this technology is a commercially viable one that may be suitable for scale-up, it is crucial to know if these devices operate effectively on larger area substrates. We therefore make large-area (1cm^2) versions of the single junctions, 2T and 4T tandems and show the current-voltage characteristics in Table 2 and Fig. S15. We find that the performance of all 1cm^2 devices remain very close to the small cells, with 2T tandems exhibiting 12.6% stabilized PCE and 4T tandems 16.0%. We attribute the excellent scalability of the devices to the PAI deposition technique allowing us to make ultra-smooth and pinhole-free films on large areas, boding well for upscaling of this approach to module fabrication in the future.

The 13.9 % PCE 2T and 18.1% 4T tandems are already in excess of the best tandem solar cells made with other similarly low cost semiconductors, such as those made with organic small molecules (world record 13 %) or amorphous and microcrystalline silicon (13.5%).(*1*, *4*) However, this is simply the starting point for perovskite multi-junction cells. Our longer term target is to push the efficiency of the sub cells of these appropriate bandgaps up towards and in excess of 20%, which will result in all-perovskite tandem cells with efficiencies in excess of 30%.

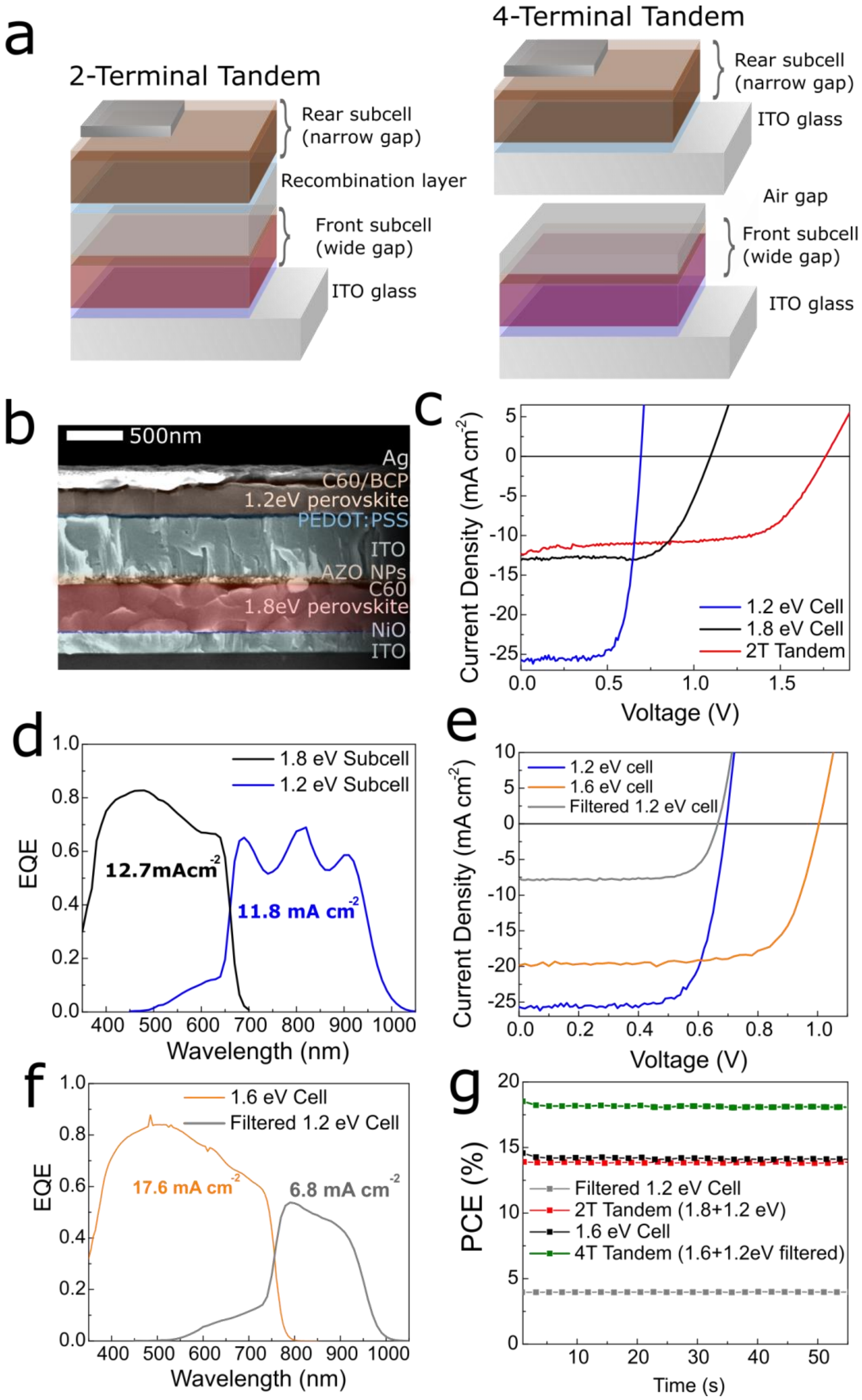
a
2-Terminal Tandem
Rear subcell (narrow gap)
Recombination layer
Front subcell (wide gap)
ITO glass
4-Terminal Tandem
Rear subcell (narrow gap)
ITO glass
Air gap
Front subcell (wide gap)
ITO glass
b
500nm
Ag
C60/BCP
1.2eV perovskite
PEDOT:PSS
ITO
AZO NPs
C60
1.8eV perovskite
NiO
ITO
c
Current Density (mA cm^{-2})
Voltage (V)
1.2 eV Cell
1.8 eV Cell
2T Tandem
d
EQE
Wavelength (nm)
1.8 eV Subcell
1.2 eV Subcell
12.7mAcm^{-2}
11.8 mA cm^{-2}
e
Current Density (mA cm^{-2})
Voltage (V)
1.2 eV cell
1.6 eV cell
Filtered 1.2 eV cell
f
EQE
Wavelength (nm)
1.6 eV Cell
Filtered 1.2 eV Cell
17.6 mA cm^{-2}
6.8 mA cm^{-2}
g
PCE (%)
Time (s)
Filtered 1.2 eV Cell
2T Tandem (1.8+1.2 eV)
1.6 eV Cell
4T Tandem (1.6+1.2eV filtered)

Figure 3. Perovskite-perovskite tandems. *a) Schematics showing 2- and 4-terminal tandem perovskite solar cell concepts. In this image devices would be illuminated from below. b) Scanning electron micrograph of the two-terminal perovskite-perovskite tandem. c) Scanned current-voltage characteristics under AM 1.5G illumination, of the two-terminal perovskite-perovskite tandem, of the 1.2 eV solar cell, and the ITO capped 1.8 ev solar cell. d) External quantum efficiency spectra for the sub-cells. e) J-V curves of a 1.2 eV perovskite, of that same solar cell filtered by an ITO capped 1.6 eV perovskite solar cell, and the ITO capped 1.6 eV perovskite solar cell, used to determine the mechanically stacked tandem efficiency. f) External quantum efficiency spectra for the mechanically stacked tandem. g) The stabilized power output tracked over time at maximum power point for the 2T perovskite solar cell, the 1.2 eV perovskite solar cell filtered by an ITO capped 1.6 eV perovskite solar cell, the ITO capped 1.6 eV perovskite solar cell, and the mechanically stacked tandem under AM 1.5G illumination. The SPO for the 1.2 eV cell and the 1.8 eV subcell are plotted in Figure S13 and given in Table 2.*

	J_{SC} (mA cm^{-2})	**V_{OC} (V)**	**FF**	**PCE (%)**	**SPO (%)**
1.2 eV Cell	25.5	0.69	0.74	13.0	**13.1**
1 cm^2 1.2 eV Cell	24.0	0.73	0.65	11.3	**11.9**
1.8 eV Cell	13.3	1.09	0.67	9.7	**9.6**
2T Tandem	12.4	1.76	0.61	13.4	**13.9**
1 cm^2 2T Tandem	12.3	1.83	0.60	13.4	**12.6**
Filtered 1.2 eV Cell	7.7	0.67	0.75	3.9	**4.0**
Filtered 1 cm^{-2} 1.2 eV Cell	5.7	0.72	0.73	3.0	**3.0**
ITO Capped 1.6 eV Cell	19.5	1.01	0.74	14.5	**14.1**
1 cm^2 ITO Capped 1.6 eV Cell	19.3	1.08	0.65	13.4	**13.0**
4T Tandem	-	-	-	18.5	**18.1**
1 cm^2 4T Tandem	-	-	-	16.4	**16.0**

Table 2*. Solar cell performance parameters corresponding to the J-V curves shown in Figure 3. Cell active areas are 0.2 or 1 cm^2. SPO = stabilized power output from MPP tracking.*

Conclusion

By designing and optimizing a new perovskite material, $FA_{0.75}Cs_{0.25}Sn_{0.5}Pb_{0.5}I_3$, we have presented an air stable 1.2 eV narrow bandgap perovskite with high charge carrier mobility and long carrier diffusion length. When incorporating this material into a planar heterojunction solar cell, we have delivered over 13% PCE. We have combined this narrow-gap cell with a wider gap 1.8eV material, $FA_{0.83}Cs_{0.17}PbI_{0.5}Br_{0.5}$ in a two-terminal tandem architecture to attain an all-perovskite tandem with ideal bandgaps. The current matching and voltage addition are effective, providing an efficiency of 14%. We also make highly efficient four terminal tandems exceeding 18% efficiency on small areas and 16% at the $1cm^2$ scale. The development of this class of efficient narrow bandgap perovskites represents a new step forward in the perovskite field, opening the possibility of highly efficient multi-junction perovskite solar cells. The key technical challenges ahead are to maximize the voltage of the front cell, increase the photocurrent in the infra-red section of the rear cell, and to push the bandgap even further in the IR in order to enable triple junction perovskite cells. These efforts, combined with industrial efforts, will lead to a new generation of thin-film PV modules with cost/efficiency ratios at a fraction of today's PV technologies, which will enable PV electricity to supersede coal, gas and oil and become the globally dominant source of power. Beyond PV, the existence of these high quality near IR absorbing and emitting perovskites may lead towards new light emitting diodes and photodetectors for communications and optics.

Acknowledgments

We thank Maximilian T. Hörantner for performing the Shockley-Quiessier calculation. The research leading to these results has received funding from the Graphene Flagship (EU FP7 grant no. 604391), the Leverhulme Trust (Grant RL-2012-001), the U.K. Engineering and Physical Sciences Research Council (Grant No. EP/ J009857/1 and EP/M020517/1), and the European Union Seventh Framework Programme (FP7/2007-2013) under grant agreement nos. 239578 (ALIGN) and 604032 (MESO). TL is funded by a Marie Sklodowska Curie International Fellowship under grant agreement H2O2IF-GA-2015-659225. We also acknowledge the Office of Naval Research USA for support. We acknowledge the use of the University of Oxford Advanced Research Computing (ARC) facility (http://dx.doi.org/10. 5281/zenodo.22558) and the ARCHER UK National Super-computing Service under the "AMSEC" Leadership project. We thank the Global Climate and Energy Project (GCEP) at Stanford University.

Author Contributions

GEE and TL conceived the project, carried out the majority of the experimental work and device making, and wrote the manuscript. TG and JTSW carried out additional film optimization and device fabrication. KAB assisted with tandem device design and optimization. RJS, RB and DJS carried out additional characterization of the $FA_{0.75}Cs_{0.25}Sn_{0.5}Pb_{0.5}I_3$ films. DPM optimized and designed the wide-gap material system. GV and FG carried out the first-principles calculations. ESP carried out photoluminescence measurements. JBP and MJ measured FTIR and FTPS. RLM, MJ and LMH carried out THz measurements and analysis. AB, BC and HGB made samples and carried out UPS and XPS measurements. WM and FM carried out ITO sputtering. MDM supervised the project. HJS conceived and supervised the project. All authors contributed to the revising and writing of the manuscript.

References

1. NREL, *Best Research-Cell Efficiencies, http://www.nrel.gov/ncpv/images/efficiency_chart.jpg* (2016; http://www.nrel.gov/ncpv/images/efficiency_chart.jpg).

2. D. P. McMeekin *et al.*, A mixed-cation lead mixed-halide perovskite absorber for tandem solar cells. *Science (80-.).* **351**, 151–155 (2016).

3. B. Azzopardi *et al.*, Economic assessment of solar electricity production from organic-based photovoltaic modules in a domestic environment. *Energy Environ. Sci.* **4**, 3741 (2011).

4. M. A. Green, K. Emery, Y. Hishikawa, W. Warta, E. D. Dunlop, Solar cell efficiency tables (Version 45). *Prog. Photovoltaics Res. Appl.* **23**, 1–9 (2015).

5. F. Meillaud, a. Shah, C. Droz, E. Vallat-Sauvain, C. Miazza, Efficiency limits for single-junction and tandem solar cells. *Sol. Energy Mater. Sol. Cells*. **90**, 2952–2959 (2006).

6. N. K. Noel *et al.*, Lead-Free Organic-Inorganic Tin Halide Perovskites for Photovoltaic Applications. *Energy Environ. Sci.* **7**, 3061–3068 (2014).

7. F. Hao *et al.*, Solvent-Mediated Crystallization of $CH_3NH_3SnI_3$ Films for

Heterojunction Depleted Perovskite Solar Cells. *J. Am. Chem. Soc.*, 150827133923001 (2015).

8. F. Hao, C. C. Stoumpos, R. P. H. Chang, M. G. Kanatzidis, Anomalous band gap behavior in mixed Sn and Pb perovskites enables broadening of absorption spectrum in solar cells. *J. Am. Chem. Soc.* **136**, 8094–8099 (2014).

9. L. Zhu *et al.*, Solvent-molecule-mediated manipulation of crystalline grains for efficient planar binary lead and tin triiodide perovskite solar cells. *Nanoscale* (2016), doi:10.1039/C6NR00301J.

10. T. Leijtens *et al.*, Overcoming ultraviolet light instability of sensitized TiO2 with meso-superstructured organometal tri-halide perovskite solar cells. *Nat. Commun.* **4**, 2885 (2013).

11. E. S. Parrott *et al.*, Effect of Structural Phase Transition on Charge-carrier Lifetimes and Defects in CH3NH3SnI3 Perovskite. *J. Phys. Chem. Lett.* (2016) (available at http://dx.doi.org/10.1021/acs.jpclett.6b00322).

12. C. C. Stoumpos, C. D. Malliakas, M. G. Kanatzidis, Semiconducting Tin and Lead Iodide Perovskites with Organic Cations: Phase Transitions, High Mobilities, and Near-Infrared Photoluminescent Properties. *Inorg. Chem.* **52**, 9019–9038 (2013).

13. J. H. Heo, S. H. Im, *Adv. Mater.*, in press, doi:10.1002/adma.201501629.

14. G. E. Eperon *et al.*, Formamidinium lead trihalide: a broadly tunable perovskite for efficient planar heterojunction solar cells. *Energy Environ. Sci.* **7**, 982 (2014).

15. S. D. Stranks, P. K. Nayak, W. Zhang, T. Stergiopoulos, H. J. Snaith, Formation of Thin Films of Organic-Inorganic Perovskites for High-Efficiency Solar Cells. *Angew. Chemie Int. Ed.* **54**, 3240–3248 (2015).

16. G. E. Eperon, V. M. Burlakov, P. Docampo, A. Goriely, H. J. Snaith, Morphological control for high performance planar thin-film perovskite solar cells. *Adv. Funct. Mater.* (2013), doi:10.1002/adfm.201302090.

17. Y. Zhou *et al.*, Room-Temperature Crystallization of Hybrid-Perovskite Thin Films via Solvent-Solvent Extraction for High-Performance Solar Cells. *J. Mater. Chem. A*. **3**, 8178–8184 (2015).

18. N. J. Jeon *et al.*, Compositional engineering of perovskite materials for high-performance solar cells. *Nature*. **517**, 476–480 (2015).

19. J.-W. Lee, H.-S. Kim, N.-G. Park, Lewis Acid–Base Adduct Approach for High Efficiency Perovskite Solar Cells. *Acc. Chem. Res.*, acs.accounts.5b00440 (2016).

20. O. D. Miller, E. Yablonovitch, S. R. Kurtz, Strong internal and external luminescence as solar cells approach the Shockley-Queisser limit. *IEEE J. Photovoltaics*. **2**, 303–311 (2012).

21. L. M. Pazos-Outon *et al.*, Photon recycling in lead iodide perovskite solar cells. *Science (80-.).* **351**, 1430–1433 (2016).

22. J. Im, C. C. Stoumpos, H. Jin, A. J. Freeman, M. G. Kanatzidis, Antagonism between Spin–Orbit Coupling and Steric Effects Causes Anomalous Band Gap Evolution in the Perovskite Photovoltaic Materials $CH_3NH_3Sn_{1-x}Pb_xI_3$. *J. Phys. Chem. Lett.* **6**, 3503–3509 (2015).

23. L. M. Herz, Charge-Carrier Dynamics in Organic-Inorganic Metal Halide Perovskites. *Annu. Rev. Phys. Chem.* **67**, annurev–physchem–040215–112222 (2016).

24. W. Rehman *et al.*, Charge-Carrier Dynamics and Mobilities in Formamidinium Lead Mixed-Halide Perovskites. *Adv. Mater.* **27**, 7938–7944 (2015).

25. N. K. Noel *et al.*, Lead-Free Organic-Inorganic Tin Halide Perovskites for Photovoltaic Applications. *Energy Environ. Sci.* **7**, 3061–3068 (2014).

26. M. B. Johnston, L. M. Herz, Hybrid Perovskites for Photovoltaics: Charge-Carrier Recombination, Diffusion, and Radiative Efficiencies. *Acc. Chem. Res.*, acs.accounts.5b00411 (2015).

27. P. Docampo, J. M. Ball, M. Darwich, G. E. Eperon, H. J. Snaith, Efficient organometal

trihalide perovskite planar-heterojunction solar cells on flexible polymer substrates. *Nat. Commun.* **4**, 2761 (2013).

28. Z. Li *et al.*, Stabilizing Perovskite Structures by Tuning Tolerance Factor: Formation of Formamidinium and Cesium Lead Iodide Solid-State Alloys. *Chem. Mater.*, acs.chemmater.5b04107 (2015).

29. J.-W. Lee *et al.*, *Adv. Energy Mater.*, in press, doi:10.1002/aenm.201501310.

30. C. Yi *et al.*, Entropic stabilization of mixed A-cation ABX 3 metal halide perovskites for high performance perovskite solar cells. *Energy Environ. Sci.* **2**, 303 (2016).

31. P. Schulz *et al.*, Interface energetics in organo-metal halide perovskite-based photovoltaic cells. *Energy Environ. Sci.* **7**, 1377 (2014).

32. C. Wang *et al.*, Electronic structure evolution of fullerene on CH3NH3PbI3. *Appl. Phys. Lett.* **106** (2015), doi:10.1063/1.4916079.

33. H. J. Snaith, Estimating the Maximum Attainable Efficiency in Dye-Sensitized Solar Cells. *Adv. Funct. Mater.* **20**, 13–19 (2010).

34. F. Hao, C. C. Stoumpos, D. H. Cao, R. P. H. Chang, M. G. Kanatzidis, Lead-free solid-state organic–inorganic halide perovskite solar cells. *Nat. Photonics*. **8**, 489–494 (2014).

35. T. Leijtens *et al.*, *Adv. Energy Mater.*, in press, doi:10.1002/aenm.201500962.

36. Z. Li *et al.*, Stabilizing Perovskite Structures by Tuning Tolerance Factor: Formation of Formamidinium and Cesium Lead Iodide Solid-State Alloys. *Chem. Mater.* **2**, acs.chemmater.5b04107 (2015).

37. T. Leijtens *et al.*, *Adv. Energy Mater.*, in press (available at http://doi.wiley.com/10.1002/aenm.201500963).

38. B. Conings *et al.*, *Adv. Energy Mater.*, in press, doi:10.1002/aenm.201500477.

39. C. D. Bailie *et al.*, Semi-transparent perovskite solar cells for tandems with silicon and CIGS. *Energy Environ. Sci.* **8**, 956–963 (2015).

40. K. A. Bush *et al.*, *Adv. Mater.*, in press, doi:10.1002/adma.201505279.

41. M. Saliba *et al.*, Cesium-containing Triple Cation Perovskite Solar Cells: Improved Stability, Reproducibility and High Efficiency. *Energy Environ. Sci.* (2016), doi:10.1039/C5EE03874J.

Supplementary Materials

Materials and Methods

Table S1 – S2

Fig S1 – S15

References